

Application of a Temporal Multiscale Method for Efficient Simulation of Degradation in PEM Water Electrolysis under Dynamic Operation

Dayron Chang Dominguez^a, An Phuc Dam^b, Thomas Richter^a, Kai Sundmacher^b, Shaun M. Alia^c

^a*Otto-von-Guericke University, Universitätsplatz
2, Magdeburg, 39106, Saxony-Anhalt, Germany*

^b*Max-Planck-Institute for Dynamics of Complex Technical Systems, Sandtorstraße
1, Magdeburg, 39106, Saxony-Anhalt, Germany*

^c*National Renewable Energy Laboratory, 15013 Denver West Parkway, Golden, CO
80401, Colorado, United States of America*

Abstract

Hydrogen is vital for sectors like chemicals and others, driven by the need to reduce carbon emissions. Proton Electrolyte Membrane Water Electrolysis (PEMWE) is a key technology for the production of green hydrogen under fluctuating conditions of renewable power sources. However, due to the scarcity of noble metal materials, the stability of the anode catalyst layer under dynamic operating conditions must be better understood. Model-aided investigation approaches are essential due to the back-box nature of the electrochemical system and the high costs of experimental long-term testing. In this work, a temporal multiscale method based on a Heterogeneous technique is applied to reduce the computational effort of simulating long-term degradation, focused on catalyst dissolution. Such an approach characterizes the problem in fast locally periodic processes, influenced by the dynamic operation and slow processes attributed to the gradual degradation of the catalyst layer. A mechanistic model that includes the oxygen evolution reaction, catalyst dissolution and hydrogen permeation from the cathode to the anode side is hypothesized and implemented. The multiscale approach notably reduces computational effort of simulation from hours to mere minutes. This efficiency gain is ascribed to the limited evolution of Slow-Scale variables during each period of time of the Fast-Scale variables. Consequently, simulation of the fast processes is required only until local periodicity is achieved

within each Slow-Scale time step. Thus, the developed temporal multiscale approach proves to be highly effective in accelerating parameter estimation and predictive simulation steps, as could be verified through the results of this article. In this way, the method can support systematic model development to describe degradation in PEMWE under dynamic operating conditions.

Keywords: Temporal Multiscale Method, Electrochemical Modelling, PEM Electrolysis, Heterogeneous Multiscale Method, Differential Equations

Introduction

Degradation of the anode catalyst layer is a major challenge in Proton Exchange Membrane Water Electrolysis (PEMWE), especially due to the need to reduce loadings of noble metal materials such as iridium. Understanding the degradation phenomena that occur within the ACL of the PEM Water Electrolyzer [1, 2] is challenging due to the “black-box” nature of such a PEMWE cell during operation, even more so under dynamic load conditions [3]. Insights are typically gained by studying the system in- and output behavior as well as by conducting post-test analysis of the system.

In situ experimental knowledge regarding the phenomenon of Ir catalyst dissolution has been acquired through the use of so-called half-cell setups, where liquid electrolytes are employed, and models are validated [4]. However, obtaining similar in situ data is challenging for the industrially relevant membrane electrode assembly (MEA) setups. Transfer of knowledge of catalyst dissolution from half-cells to full-cells is not straight forward [5, 6].

Therefore, mathematical modelling is of essential importance to understand the physico-chemical processes occurring inside the cell. Since the early 2000s modelling processes in PEMWEs has been used as a tool to make up for shortfalls in such a closed schema [7, 8]. An extensive classification of different ways of modelling PEMWE can be found in [9]. Some are focused on the understanding of the phenomena under various conditions such as high-pressure water electrolysis [10, 11] or hydrogen permeation [12, 13, 14]. Additionally, models ranging from 0D to 3D of PEMWEs have been developed based on physical laws to comprehend processes such as mass transport [15, 16], fluid behavior through the Porous Transport Layer (PTL) [17, 18, 19, 20] among others.

In the area of performance characterization and control system development, there are works like [21, 22, 23, 24, 25, 26], mainly focus on analysis

of experimental results and long-term durability evaluation. The authors utilized fitting techniques based on experimental data to identify parameters and optimize the performance of PEMWEs using often “black-box” models. In this regard, the machine learning era unfolds data-driven simulating techniques which accelerate the fitting processes due to its computational efficiency [27].

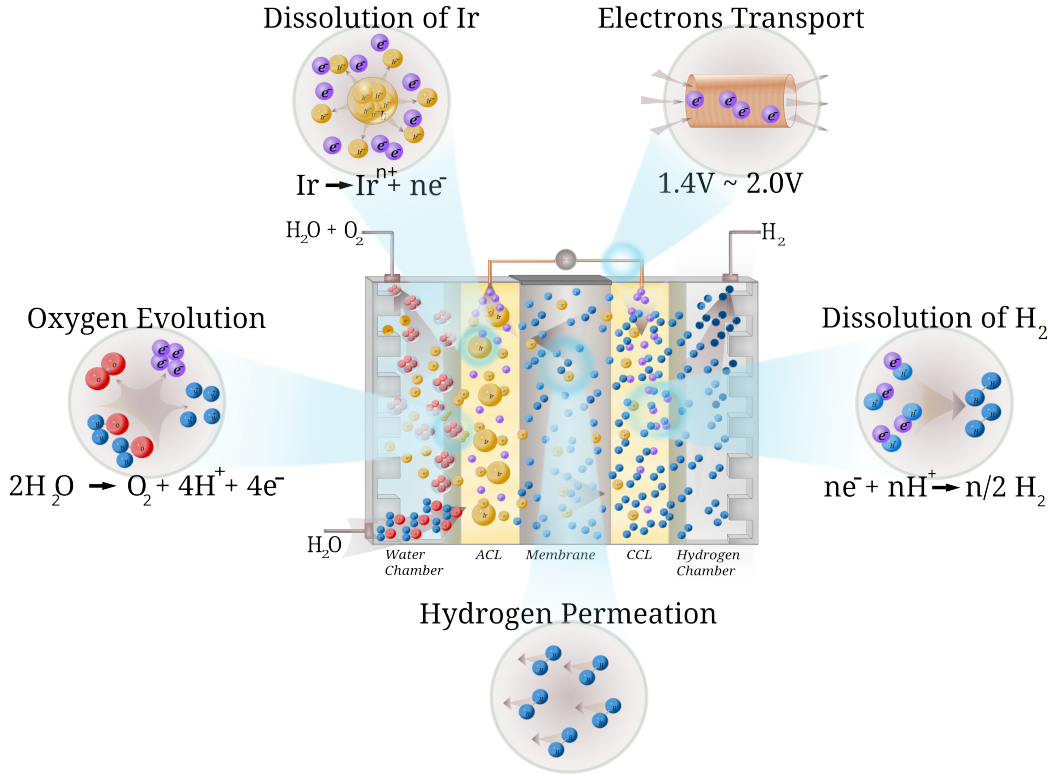


Figure 1: Theoretical schema of the processes of the PEMWE that are taken into consideration in the proposed model.

Models have been developed for PEMWE in which multiscale analysis has been applied in order to better resolve spatial dimensions [28, 29, 30, 31]. In this study a white-box methodology for modelling the dissolution phenomena inside the PEMWE ACL shall be developed (Figure 1). This will be numerically supported by applying a temporal multiscale method for the time dimension in order to reduce computational effort.

This technique has been used to describe long-term effects in the interac-

tion of processes of different time scales in different applications as is shown in [32, 33]. In this way, the Heterogeneous Multiscale Method (HMM) [34] is one of the most promising options to efficiently decouple the micro-scale and macro-scale of the problem solving the last one based on temporal averaging of the first one. A review of these techniques can be found in [35, 36] where authors compare the HMM with other techniques, mainly applied for ODEs or to spatial multiscales.

In [37] a description of a computational temporal multiscale method is derived. It assumes that the underlying fast process has a time quasi-locally periodic solution if the influence of the Slow-Scale solution is fixed during the slow time step. Therefore, only solving the Fast-Scale variables until such a time quasi-locally periodic is achieved allows the Slow-Scale variables to have very large time steps and accelerate the simulations in about 10^4 times.

In this paper a simple physico-chemical model of Iridium catalyst dissolution is proposed in Section 1. It is shown that with the introduction of a numerical temporal multiscale method in Section 2, the simulation time of the PEMWE ACL long-duration stability tests is drastically reduced. In Section 3 the method is numerically analyzed showing how to overcome the challenges of the stiffness nature of the problem. The model parameters are fitted to experimental data of two dynamic operation profiles [38] of accelerated stress tests (see section 4). A good fit of model simulation with experimental data is achieved. The model with the fitted parameters is then used to predict other dynamic operation profiles. The simulation is compared to experimental data and implications on the hypothesized electrochemical model are discussed.

Overall, the aim of this work is to demonstrate how the introduction of a temporal multiscale approach, facilitates the systematic development of a mathematical model capable of describing the effects of different dynamic operational profiles on catalyst degradation in PEMWE.

1. Anode Catalyst Layer degradation model

In this section, the electrochemical degradation model of the ACL during the operation of the PEMWE is described. The dissolution model is presented in Section 1.1, and an important influence of hydrogen is assumed, as it can chemically reduce the Ir oxide, thus leading to its destabilization during dynamic operation of PEMWE [13, 39]. Therefore, a transport model has

been developed and implemented to describe the dynamic permeation process of hydrogen from the cathode to the anode side which will be discussed in section 1.2.

1.1. Iridium dissolution model

To describe the dissolution process of Ir, based on knowledge and understanding from previous works in literature, a simple mechanistic model is hypothesized and implemented. The model considers nano-particles of Irid-

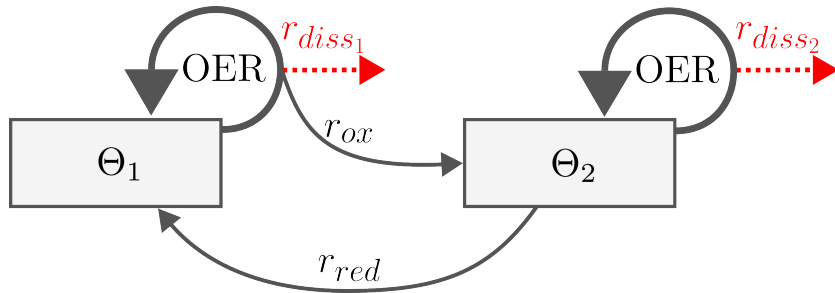


Figure 2: Theoretical representation of the electrochemical model for corrosion of the material in the ACL.

ium in which the catalyst material surface can be in two different chemical oxidation states as shown in Figure 2. They can be either in a reduced or an oxidized state. Θ_1 and Θ_2 correspond to the more reduced and the more oxidized state, respectively.

Figure 2 illustrates the schematic of Iridium dissolution model which was implemented in this work. It is well known that catalyst dissolution and OER are closely coupled phenomena. An unstable state of the catalyst surface during the OER reaction cycle leads to catalyst dissolution [40, 41, 5].

In this model it is assumed that the surface is generally in an oxidized state during the considered operation of PEMWE at OER potentials. However, hydrogen which permeates from the cathode to the anode side can reduce the oxidation state of the active site on the catalyst surface. Thus, this reduction converts it from the state Θ_2 to the state Θ_1 (r_{red}).

Nevertheless, the OER leads to dissolution of those chemically reduced active sites. As a result, the Ir oxide lattice structure underneath the dissolved catalyst species becomes exposed to the surface. The surface state Θ_1 then reverts back towards the more stable state Θ_2 (r_{ox}). However, the dissolution of catalyst species leads to a loss of catalyst material leading to a loss of

Electrochemical Surface Area (ECSA) and a gradual decline in electrolyzer performance over time.

The catalyst surface in state Θ_2 is more stable than in state Θ_1 . However, due to the inherent coupling of catalyst dissolution and OER [42, 40], the catalyst can dissolved also in the former state. Therefore, two dissolution pathways are considered in the implemented model, as shown in Figure 2.

The involvement of hydrogen in the dissolution of catalyst material may influence the observed ACL degradation rates. This is especially notable under different dynamic operation conditions, as these conditions strongly influence the dynamic behavior of oxygen and hydrogen partial pressure in the ACL. A high current density results in a low hydrogen partial pressure as evolved oxygen generates a flushing effect on the ACL. On the other hand, the decrease in current density leads to a dynamic accumulation of hydrogen in the ACL, attributable to the prior storage of permeating hydrogen within the membrane.

The implemented mathematical model can be expressed by the following system of ordinary differential (ODE) equations:

$$\frac{d\Theta_1}{dt} = 2k_r(1 - \Theta_1)^2 (C_{H_2}^{ACL} RT) - \frac{\Theta_1}{\gamma} k_{diss1} e^{fE^{ACL}} \quad (1)$$

$$\frac{dC_{O_2}^{ACL}}{dt} = V_{ACL}^{-1} \left[\frac{i}{z_{O_2} F} - A_{geo} F_{O_2}^{PTL} \right] \quad (2)$$

$$\frac{dC_{H_2}^{ACL}}{dt} = \frac{A_{geo}}{V_{ACL}} [F_{H_2}^{Mem} - F_{H_2}^{PTL}] \quad (3)$$

$$\frac{dN_{Ir}^{np}}{dt} = -\frac{A_{Ir}^{act}(N_{Ir}^{np}(t))}{A_{geo}} [\Theta_1 k_{diss1} + (1 - \Theta_1) k_{diss2}] e^{fE^{ACL}} \quad (4)$$

The origin and meaning of the variables and terms in this system of ODEs shall be described in the following sections. Θ_1 describes the fraction of active sites which are in state number 1 (see 2). The first term of (1) expresses the reduction rate with its reaction rate constant k_r .

The reduction kinetics depends on the pressure of hydrogen in the ACL since it occurs via chemical reduction with hydrogen and is written via elementary reaction kinetic formulation. The modelled reduction process may be described by the chemical reaction equation $2IrO_2 + H_2 \rightarrow 2HIrO_2$. The hydrogen partial pressure can be calculated using the ideal gas law:

$$P_{H_2}^{ACL} = C_{H_2}^{ACL} RT, \quad (5)$$

with R and T being the universal gas constant and the temperature, respectively. $C_{H_2}^{ACL}$ is the concentration of hydrogen in the ACL and is given in mol/m^3 . The hydrogen-induced reduction reaction leads to a conversion of active sites from state Θ_2 to the state Θ_1 .

On the other hand, the right term of equation (1) represents the conversion of sites in state Θ_1 back to the state Θ_2 . This is explained by the dissolution of reduced and destabilized sites, exposing the Ir oxide species that were originally located underneath the dissolving sites. k_{diss1} is the dissolution rate constant for the sites in Θ_1 state. γ is the number of active sites per surface area of the Ir oxide nano-particles and a value of $1.121 \cdot 10^{-4} mol/m^2$ is used for the simulation [43]. E^{ACL} is the potential applied on the ACL, and $f = F/(RT)$, where F is the Faraday constant $96485 C/mol$.

In terms of spatial direction, the ACL is modelled zero-dimensionally. The balance of the gases it is shown in the equations (2) and (3). The O_2 concentration is balanced by a source and a flow term. Within the source term, i represents the current density (A/m^2) and z_{O_2} is equal to 4, corresponding with the number of electrons transferred per evolved oxygen molecule. The other term of equation (2) defines the flow of O_2 from the ACL to the porous space inside the adjacent PTL domain. These fluxes can be described by:

$$F_{O_2}^{PTL} = F^{tot} X_{O_2} \quad \text{and} \quad F_{H_2}^{PTL} = F^{tot} X_{H_2}, \quad (6)$$

where F^{tot} is the total gas flow out of the ACL and X_{O_2} and X_{H_2} are the oxygen and the hydrogen fraction in the gas phase, respectively. These fractions can be calculated by:

$$X_{O_2} = \frac{P_{O_2}^{ACL}}{P_{H_2}^{ACL} + P_{O_2}^{ACL}} \quad \text{and} \quad X_{H_2} = \frac{P_{H_2}^{ACL}}{P_{H_2}^{ACL} + P_{O_2}^{ACL}}. \quad (7)$$

The total gas flow F^{tot} is calculated using the following equation:

$$F^{tot} = k_{ACL} ((P_{O_2}^{ACL} + P_{H_2}^{ACL}) - P^{atm}). \quad (8)$$

The pressure difference serves as the mechanical driving force for the gas flow out of the ACL. The parameter k_{ACL} is a mass transport coefficient and its inverse describes the resistance of gas transport out of the ACL domain. Although, in reality, this transport resistance is distributed spatially across the ACL thickness, for the sake of simplicity, this work assumes discrete occurrence at the interface between the ACL and PTL domains.

A value of k_{ACL} can be determined using the Darcy-Weißbach equation, assuming a pore diameter of 52 nm [38] and a correction for the friction factor of 0.005 [44]. An ACL thickness of 1 μm is assumed for the ACL with low catalyst loading [38]. P^{atm} is the atmospheric pressure which can be considered as the pressure level inside the pores of the PTL domain.

Equation (3) considers output and input flows. The outflow is defined as $F_{\text{H}_2}^{\text{PTL}}$ in equation (6). The input flow $F_{\text{H}_2}^{\text{Mem}}$ which comes from the membrane domain will be explained in the following Subsection 1.2.

Equation (4) describes the temporal evolution of the amount of Ir in the form of nanoparticles ($N_{\text{Ir}}^{\text{np}}$ measured in moles) within the ACL due to the two previously described dissolution mechanisms. The ECSA, defined by $A_{\text{Ir}}^{\text{act}}$, is calculated based on

$$A_{\text{Ir}}^{\text{act}} = \eta_{\text{np}}^{\text{act}} 4\pi r_{\text{np}}^2 \quad \text{and} \quad r_{\text{np}} = \sqrt[3]{\frac{3N_{\text{Ir}}^{\text{np}} M_{\text{Ir}}}{4\pi \rho_{\text{Ir}} \eta_{\text{np}}^{\text{act}}}}. \quad (9)$$

The variable $\eta_{\text{np}}^{\text{act}}$ represents the number of active nanoparticles, while the radius r_{np} denotes their size. Additionally, parameters such as the molar mass of Iridium, denoted as M_{Ir} (in [g/mol]), and its density ρ_{Ir} (in [g/m³]) are present in the formulation.

In the kinetics a linearity between Ir catalyst dissolution and OER at higher current densities is included. This linearity results in the same factor in front of the potential within the exponent of the rate expression.

1.2. Transport of hydrogen through the membrane

Due to the electrochemical polarization of the catalyst layer, hydrogen is evolved in the CCL. In previous studies, it has been found that this creates a supersaturation of hydrogen in the CCL, resulting not only in the transport of hydrogen in the cathode channel direction but also the permeation of hydrogen to the anode side [45]. This is schematically shown in Figure 3. In this work, the transport is modelled via a Partial Differential Equation which considers the time-dependent diffusion of hydrogen over the membrane domain as

$$\partial_t C_{\text{H}_2}^{\text{MEM}}(x, t) - D_{\text{H}_2}^{\text{eff}} \partial_{xx} C_{\text{H}_2}^{\text{MEM}}(x, t) = 0. \quad (10)$$

The PDE is discretized and solved using the Finite Element Method in a one-dimensional domain, considering $D_{\text{H}_2}^{\text{eff}}$ as the effective hydrogen diffusion coefficient of the membrane.

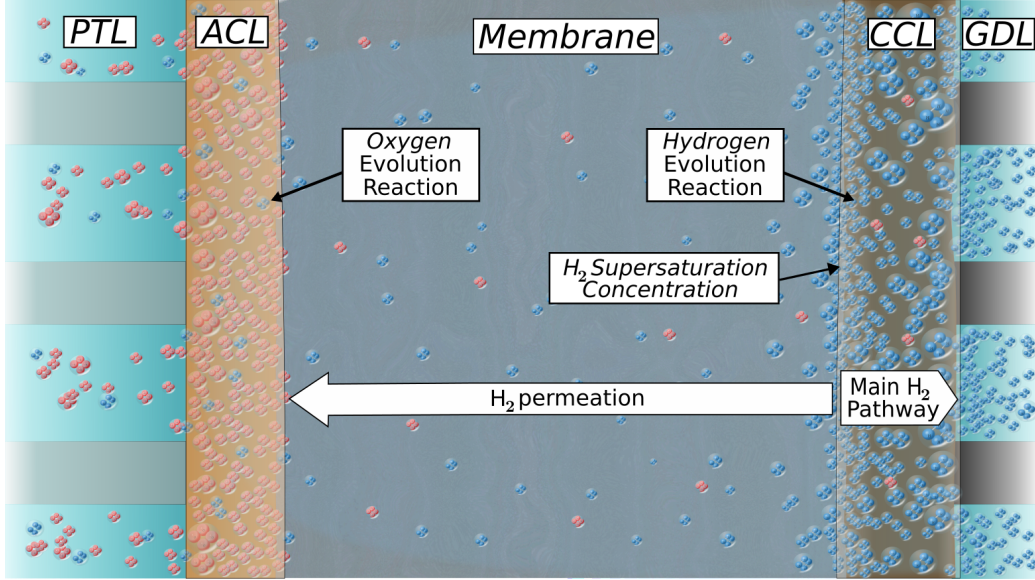


Figure 3: The sketch shows a section of the PEMWE consisting of the membrane at the center and the ACL and the CCL at the sides. In the cathode catalyst layer most of the evolved hydrogen is transported to the cathode outlet. However, a small fraction of hydrogen permeates into the other direction towards the anode side. In the ACL oxygen is evolved and a small volumetric fraction is constituted by hydrogen.

The boundary condition at the CCL side was implemented as a Dirichlet boundary condition. For simplicity, this can be done by assuming quasi-steady-state conditions at the CCL and therefore calculating the supersaturation concentration based on the following equation ([45]):

$$C_{\text{H}_2}^{\text{CCL}}(t) = \frac{\frac{i}{2F} + k_l C_{\text{H}_2}^{\text{Henry}}(t)}{k_l + \frac{D_{\text{H}_2}^{\text{eff}}}{\delta^{\text{MEM}}}}. \quad (11)$$

On the rhs, the first term of the numerator represents the H_2 evolution which depends on the current density i . For the mass transfer coefficient k_l , which describes the transport from the reaction local to the cathode GDL domain, a value of 10^{-4}m/s is used, taken from the same source. $C_{\text{H}_2}^{\text{Henry}}$ is the theoretical saturation concentration of dissolved hydrogen assumed from Henry's law without mass transfer limitations. The membrane δ^{MEM} is considered one-dimensionally in space and discretized from 0 to the membrane thickness of $L = 183 \mu\text{m}$.

On the other side, the boundary conditions for the membrane and the ACL are defined via Neumann boundary conditions

$$D_{H_2}^{\text{eff}} \partial_x C_{H_2}^{\text{MEM}}(0, t) = k_{H_2}^{\text{MEM}} RT (C_{H_2}^{\text{MEM}}(0, t) - C_{H_2}^{\text{ACL}}(t)). \quad (12)$$

For the mass transfer coefficient $k_{H_2}^{\text{MEM}}$ a very high value of 10^{-10} is chosen and therefore, effectively, the resistance directly at the interface of membrane and ACL domain is considered negligible. Note that the entire equation has been divided by the diffusion coefficient, which is consequently combined into the model parameter $k_{H_2}^{\text{MEM}}$ (unit $1/m$).

The factor RT comes from the original definition of the transport rate coefficient, which is based on the pressure difference as the driving force. The ideal gas law, as given by equation (5), can be used to express the same term via the concentration difference. $C_{H_2}^{\text{MEM}}(0, t)$ is the estimated concentration of hydrogen at the first element of the discretized membrane over time and the concentration inside the ACL is given by the variable $C_{H_2}^{\text{ACL}}$. The flux between the membrane and the ACL $F_{H_2}^{\text{Mem}}$ in equation (3) is calculated by:

$$F_{H_2}^{\text{Mem}}(t) = k_{H_2}^{\text{MEM}} RT (C_{H_2}^{\text{MEM}}(0, t) - C_{H_2}^{\text{ACL}}(t)). \quad (13)$$

This relationship is employed to couple both problems: the ACL modelled by an ODE system and membrane domain by a PDE. The coupling is achieved through a Fixed Point Iteration Method as explained in Section 3.

2. Temporal Multiscale Method for solving the degradation model

Upon closer examination of the complete problem described by equations (1 - 4, 10) a difference in time scales between equation (4) and the others becomes noticeable. The process of dissolution, in fact, takes hours to undergo a measurable change in its state. In contrast, the remaining equations describe very fast processes as kinetics (represented by Θ_1 and Θ_2) and the changes in the concentrations of O_2 and H_2 in the ACL. As a matter of effect, those occur in time lapses less than a second.

The assumed magnitudes for the mentioned equations are responsible for the time scale distinctions. The first term of (1) is approximately 10^{-11} taking into account that $k_r \approx 10^{-14}$, $0 \leq \Theta_1 \leq 1$ and the maximum value of $C_{H_2}^{\text{ACL}}$ is approximately 0.5 bar. The second term has a magnitude of 10^{-12} due to $k_{\text{diss}_1} \approx 10^{-25}$, resulting in a total magnitude of 10^{-12} for the entire

equation. In the case of the equation (4), the constant k_{diss_2} is assumed to be around 10^{-37} , resulting in a total magnitude of approximately 10^{-5} .

Therefore, there exists a proportionality between the variables which can be approximated by $\varepsilon \approx 10^{-7}$. This reveals an underlying temporal multi-scale structure of the complete problem, as proposed by Weinan in [46], with variables categorized into Fast-Scale and Slow-Scale from equations (1 - 3, 10) and (4) respectively. Furthermore, the Slow-Scale is $O(1)$ with respect to the Fast-Scale through ε .

Moreover, the Fast-Scale processes also display a local quasi-periodic behavior due to the input of the potential. If the slow variable would not further evolve, a periodic-in-time forcing would result in a periodic response. Thus, these profiles simulate the oscillatory behavior resulting from real-world degradation of PEMWEs in operation. Then, during a P period of time there are not significant changes of the Slow-Scale variables.

A direct simulation of such a temporal multiscale problem is not efficient. Resolving the complete time interval with time steps of less than a second (e.g. $\Delta k = 10^{-2}s$) would result in excessive computational effort although the slow process, which is the one of most interest, is hardly changing. We therefore utilize a temporal multiscale algorithm that is based on the heterogeneous multiscale method [34, 47] and that aims at decoupling slow and fast scale.

The first step of decoupling is to derive an effective equation by averaging the slow process (4) over one period P . Second, instead of resolving the fast process dynamically in time, it is localised by fixing the slow variable $N_{I_r}^{np}$ and by replacing the Fast-Scale feedback by the periodic-in-time limit cycle of (1 - 3, 10) which can be numerically approximated without simulating the complete history of the fast scale variables. By this decoupling, a temporal multiscale method is obtained that allows to step forward the coupled temporal multiscale problem with very large time-steps. We refer to [37, 48] for details.

Taking advantage of this particular structure of the problem and the theory of Averaging of the multiscale problems it is possible to approximate the complete problem with its corresponding temporal multiscale problem as in the next subsection 2.1 will be explained.

2.1. Temporal Multiscale Method

Based on the stated, the Slow-Scale variables of the approximated temporal multiscale problem are defined over $t \in [0, T] \subset \mathbb{R}$ having ΔK as a large

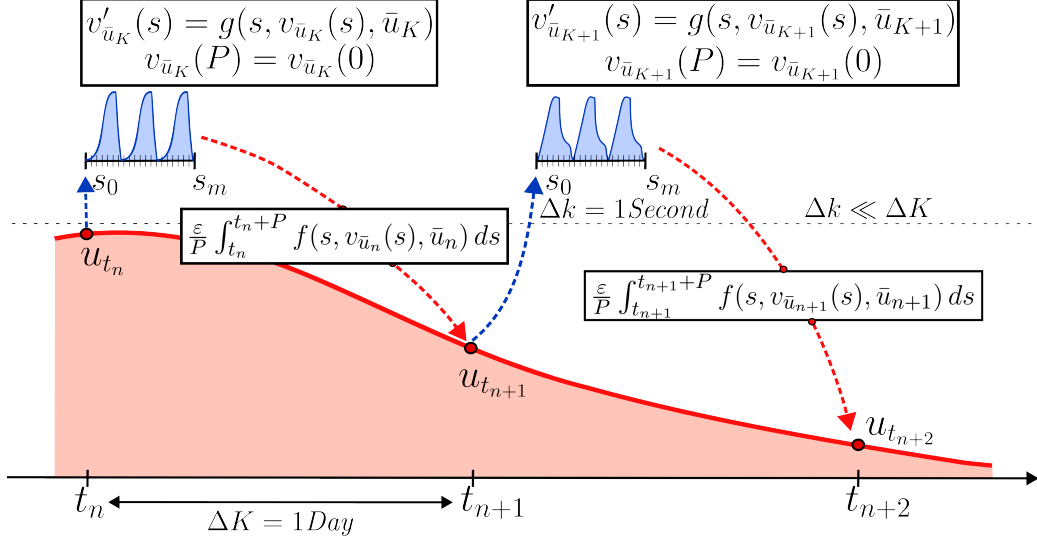


Figure 4: Schema of the temporal multiscale method.

time step size. In the case of the Fast-Scale variables, if P is established as the period and $0 \leq m \leq (T - \Delta K)/\Delta K$, then these variables will be defined over $s \in [t_K + \Delta K + nP, t_K + \Delta K + (n + 1)P]$ for $0 \leq n \leq (\Delta K - P)/P$ and $t_K = m\Delta K$ with a small time step size $\Delta k \ll \Delta K$. The new problem is written as follows:

Find $\bar{N}_{Ir}^{np}(t)$ that approximates $N_{Ir}^{np}(t)$ and is the solution of

$$\frac{d\bar{N}_{Ir}^{np}}{dt} = -\frac{\varepsilon}{P} \int_{t_K+nP}^{t_K+(n+1)P} \frac{A_{Ir}^{\text{act}}}{A_{geo}} \left[\hat{\Theta}_1(s) k_{\text{diss}_1} + (1 - \hat{\Theta}_1(s)) k_{\text{diss}_2} \right] e^{fE^{\text{ACL}}(s)} ds \quad (14)$$

so that for all K there exists $n \in \mathbb{N}_0$ and the interval $[t_K+nP, t_K+(n+1)P] \subset$

$[t_K, t_{K+1}]$ such that the equations of the Fast-Scale

$$\frac{d\hat{\Theta}_1(s)}{ds} = 2k_r(1 - \hat{\Theta}_1(s))^2 \left(\hat{C}_{H_2}^{ACL}(s) RT \right) - \frac{\hat{\Theta}_1(s)}{\gamma} k_{\text{diss1}} e^{fE^{ACL}(s)} \quad (15)$$

$$\frac{d\hat{C}_{O_2}^{ACL}(s)}{ds} = \frac{A_{Ir}^{\text{act}}(\bar{N}_{Ir}^{np}(t))}{V_{ACL}} \left[\frac{i}{z_{O_2}F} - F_{O_2}^{PTL}(s) \right] \quad (16)$$

$$\frac{d\hat{C}_{H_2}^{ACL}(s)}{ds} = \frac{A_{\text{geo}}}{V_{ACL}} [F_{H_2}^{\text{Mem}}(s) - F_{H_2}^{\text{PTL}}(s)] \quad (17)$$

$$\partial_s \hat{C}_{H_2}^{\text{MEM}}(x, s) = D_{H_2}^{\text{eff}} \partial_{xx} \hat{C}_{H_2}^{\text{MEM}}(x, s), \quad (18)$$

with the same initial conditions as the complete problem, are satisfied in each chosen interval and their solution is locally quasi-periodic.

The choice of ΔK is conditioned by the prior choice of Δk and the previously calculated scaling constant ε , such that $\Delta K \approx \Delta k/\varepsilon$. In this case, Δk is set to 10^{-2} seconds to ensure stability over the Fast-Scale resolution. Since the experimental data used for validation was sampled in days, it was convenient to choose $\Delta K = 1$ day, which is approximately 10^5 seconds and satisfies the mentioned temporal scale relation.

In order to simplify the notation some new symbols have been included. The $(\bar{\cdot})$ accent will be understood as the average of the function, in this case the Slow-Scale variable. On the other hand, $(\hat{\cdot})$ will represent the dependency

$$\hat{v} = (\hat{\Theta}_1, \hat{C}_{O_2}^{ACL}, \hat{C}_{H_2}^{ACL}, \hat{C}_{H_2}^{\text{MEM}}) \quad (19)$$

in which function v could be any of the Fast-Scale variables (in case of variable $\hat{C}_{H_2}^{\text{MEM}}$, x is also included).

3. Numerical implementation

The numerical solution of the proposed problem in Section 2 is achieved by the implementation of the general temporal multiscale method shown in Algorithm 1. The main idea is to solve the Fast-Scale problem using a *semi-implicit* method with a fixed u_K solution over the interval $[t_K, t_K + \Delta K]$, until it reaches a locally quasi-periodic solution \hat{v}_{u_K} with an error tolerance $\|tolp\|_{\infty}$. Then, the periodicity convergence criteria is defined as the infinite norm of the component-wise absolute errors for each Fast-Scale variable of the ACL. After that, u_{K+1} is obtained by integrating the averaged Slow-Scale equation over the time interval which \hat{v}_{u_K} is defined.

Algorithm 1 General temporal multiscale method for PEMWE dissolution problem

Require: $u_K = \bar{N}_{I_r}^{np}(t_0)$, $\hat{v}_{u_K} = v_0$

1: **for** $K = 0, \dots, N - 1$ **do**

2: *Find the solution of the Fast-Scale equations \hat{v}_{u_K} with fixed u_K such that for $n > 0$:*

$$\|\hat{v}_{u_K}(t_K + nP) - \hat{v}_{u_K}(t_K + (n + 1)P)\| < \text{tol}p$$

3: *Find u_{K+1} integrating the average of the Slow-Scale equation in the interval of the Fast-Scale solutions \hat{v}_{u_K} such that:*

$$u_{K+1} = u_K - \frac{\varepsilon \Delta K}{P} \int_{t_K + nP}^{t_K + (n+1)P} \left[\hat{\Theta}_1(s) k_{\text{diss}_1} + (1 - \hat{\Theta}_1(s)) k_{\text{diss}_2} \right] e^{fE^{\text{ACL}}(s)} ds$$

4: **end for**

5: **return** u_{K+1}

In order to solve the Fast-Scale problem the ODE System (15 - 17) coupled to the Transport Problem (18) must be solved. The solution of the Transport Problem was achieved by the application of a one dimensional time implicit Finite Element Method. Approximation of integrals of the mass and stiffness matrices were carried out by applying the trapezoidal method. For time integration the implicit backward Euler method was implied.

On the other hand, due to the stiff features of the problem, the ODE System mentioned before was solved applying an second-order backward differentiation formula scheme implemented in the ‘ode’ function of the ‘integrate’ module of the scientific computing library ‘scipy’ [49], available in the Python programming language. Back in Section 1, it was explained how hydrogen coming from the membrane could drastically permeate the ACL, and this is precisely what causes a jump in the solutions, making it more difficult to solve with explicit methods, which will need time step adaptivity and therefore longer computation time.

Coupling both problems in each time step Δk was accomplished by first solving the ODE system (15 - 17) implicitly with step size Δk , keeping u_K and $\hat{C}_{\text{H}_2}^{\text{MEM}}(t_K)$ fixed. Afterwards, the Transport Problem (18) is solved considering the solutions of the system (15 - 17) corresponding to t_K and t_{K+1} . Once a locally quasi-periodic solution \hat{v}_{u_k} is found, then the Slow-Scale equation is integrated. The integration method used for this purpose is the Adams-Bashforth second order method.

4. Results and discussion

The dynamic operation profiles, as well as experimental data, are taken from Alia et al. [38]. The cyclic voltammetric charge, which was systematically measured in this work, is used as a metric for the electrochemical surface area of the PEMWE device. In this experimental investigation, five dynamic operation profiles were applied in which the cell potential was controlled (Figure 5). These long-term experiments were conducted for 525 hours of operation.

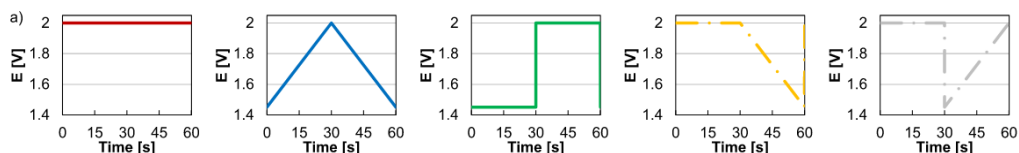


Figure 5: Experimental data of five test profiles acquired from [38]. They are named from left to right: hold, triangle-wave, square-wave, sawtooth-up and sawtooth-down profiles.

4.1. Temporal Multiscale simulation

A comparison between the fully-resolved and the temporal multiscale problems was made to verify the accuracy of the approximation that could be achieved with the multiscale approach. The simulations were run simulating 21 days of operation of the PEMWE with initial ECSA = $3.25 \cdot 10^{-2} m^2$, period of 60 seconds and, as was shown in Section 2.1, Δk and ΔK are chosen as 10^{-2} seconds and 24 hours respectively.

In Table 1, the results of this comparison, considering the already fitted parameters, are tabulated. From it, we see that the average ratio of computational time between these two methods is approximately 2.82 orders of magnitude, which means that the temporal multiscale method is around thousand times faster than the fully-resolved one on average. The best computational time for the fully-resolved problem is about 6.4 days, which, compared with the 21 minutes that the longest temporal multiscale simulation took, represents a significant computational reduction. Thus, approximately 1.25 simulation days are computed per 1 minute of computation for the temporal multiscale method.

The maximum mean squared error between these two sets of simulation results is approximately $5.52 \cdot 10^{-4}$, which is very small considering the enor-

Table 1: Computational time and mean squared error (MSE) of the results for the fully resolved problem and the temporal multiscale method (FRP and TMS) across the five experimental profiles [38] for 21 simulated days.

Experiment profiles	Computational time		MSE($N_{\text{Ir}}^{\text{np}}, \bar{N}_{\text{Ir}}^{\text{np}}$)
	FRP(days)	TMS(min)	
Hold	8.6	19.09	$7.87 \cdot 10^{-06}$
Square-wave	6.8	13.29	$2.46 \cdot 10^{-04}$
Triangle-wave	6.4	13.46	$5.39 \cdot 10^{-06}$
Sawtooth Down	8.0	16.84	$3.00 \cdot 10^{-05}$
Sawtooth Up	8.2	21.06	$5.52 \cdot 10^{-04}$

mous computational reduction made. This shows that the temporal multiscale method is accurate enough to be used instead of the fully-resolved one for approximating the long-term effects of the dissolution of Iridium when a PEMWE is operated. This property is ideal for estimating parameters efficiently as will be shown in Section 4.2.

4.2. Parameter fitting

Regarding fitting the parameters of the model, a single set of parameters k_r and k_{diss_2} , was estimated using data obtained from hold and square-wave profiles. The data from the other profiles was used as a test set. The objective function of the resulting optimization problem is expressed as

$$\sigma^* = \arg \min_{\sigma \in \Omega \subset \mathbb{R}^2} \frac{1}{T} \int_0^T (S_{\text{HP}}(t) - u_{\text{HP}}(t; \sigma))^2 + (S_{\text{SWP}}(t) - u_{\text{SWP}}(t; \sigma))^2 dt, \quad (20)$$

where Ω is the space of feasible solutions of the form $\sigma = (k_r, k_{\text{diss}_2})$, S_{HP} and S_{SWP} the sampled data from hold and square-wave profile and u the Slow-Scale variable for each case.

For the fitting procedure, a variant of the Simulating Annealing Optimization Method called Simple Serializable Set from [50] was applied. In this way, a computer server with 128 cores and 260 GB of memory ram was used to widely spread the search around partial solutions, running 128 simultaneous simulations for each set of parameters in the search neighborhood for each iteration of the method. At the end of the fitting procedure the values $k_r^* = 2.437792 \cdot 10^{-14}$ and $k_{\text{diss}_2}^* = 1.947001 \cdot 10^{-37}$ have been identified. The mean squared errors of Table 1 show the achieved accuracy.

4.3. Evaluation of the Model Performance with Experimental Data

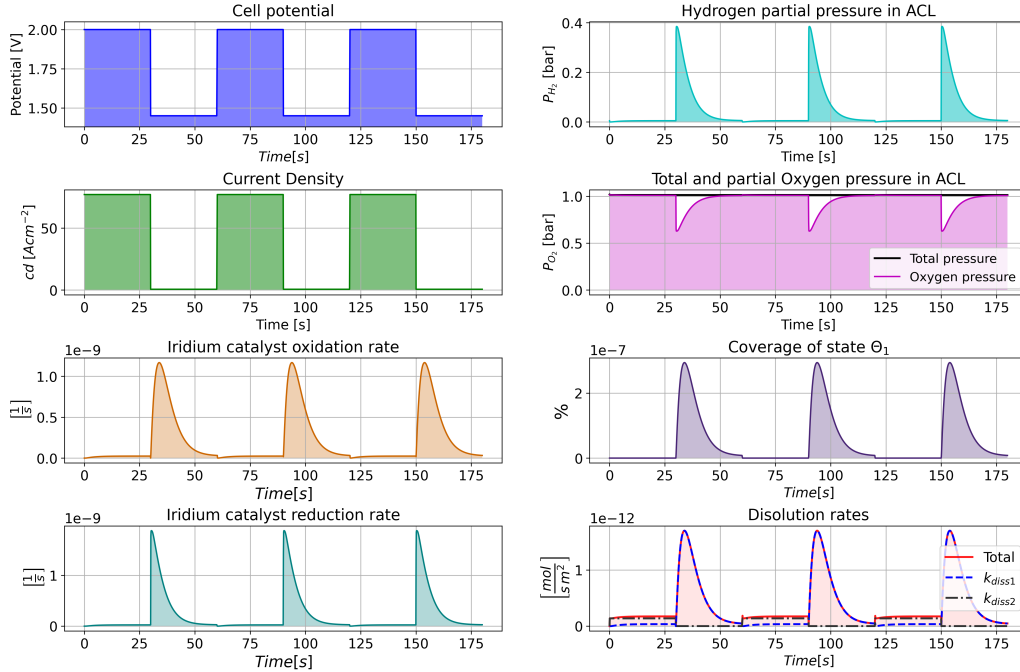


Figure 6: Fast-Scale variables for the square-wave profile simulation for the first 3 periods ($0 \leq t \leq 180$ seconds). The solution of the transport of hydrogen through the membrane is shown in the

Multiple output variables were obtained for each Fast-Scale variable. The Fast-Scale variables of the hold profile exhibit steady-state behavior almost throughout the entire duration. To provide a more insightful comparison, the results of the square-wave profile are presented in Figure 6 and Figure 7, as this profile, along with the Hold profile, was chosen for fitting the model parameters.

In Figure 6, abrupt changes in all variables are observable at every period, specifically at 30 seconds after the start of each. These changes result from sudden drops in the applied cell potential, which is also the source of the *stiffness* discussed in Sections 1 and 3.

With respect to the transport of hydrogen in the membrane, Figure 7 illustrates various stages of hydrogen concentration profile during the last period shown in Figure 6. Graphs (a) and (b) indicate the build up of the pressure during the rise of potential up to 1.45V. An initial stage of potential

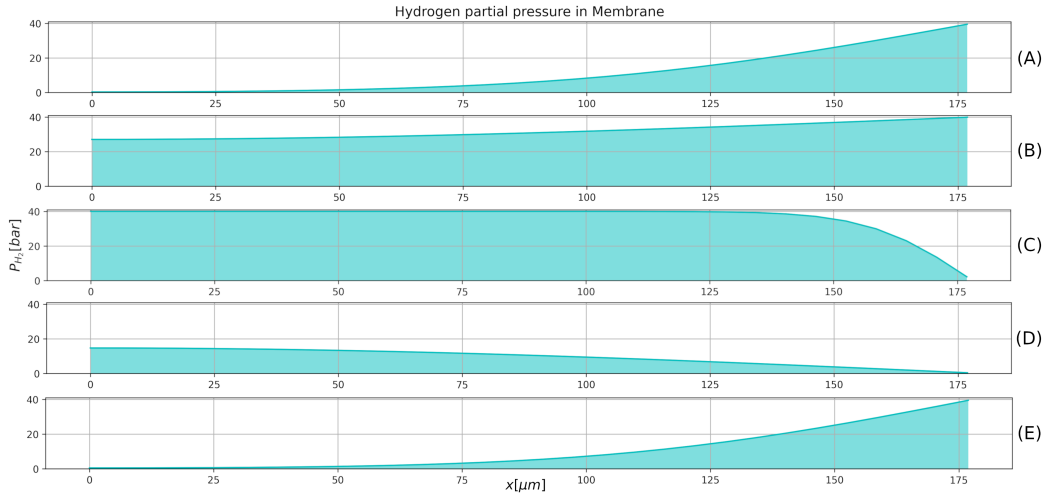
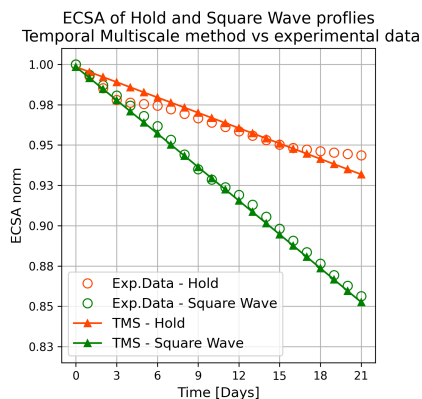


Figure 7: The Fast-scale solutions of the hydrogen transport problem in the membrane for the period $t \in [120, 180]$ sec. The graph (a) is the state of the concentration of hydrogen at $t = 120$ sec, (b) at $t = 125$ sec, (c) at $t = 150$ sec, (d) at $t = 155$ sec and (e) at $t = 180$ sec respectively.

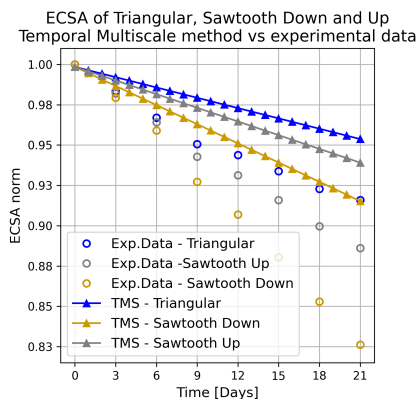
drop is shown in (c), where the hydrogen concentration decreases in the CCL due to the drop in current density. In (d), the amount of hydrogen stored in the membrane has been almost completely transported out. Finally, in (e) a high current density was restarted, and the entire process repeats itself.

The Slow-Scale variable is presented in Figure 8. It is illustrated how the ECSA decays over time for experimental data and the model simulation. It can be observed that, through the described fitting procedure, a single set of parameters has been obtained. The use of the latter results in a good agreement between the simulation and experimental data for both the hold and square-wave operation profiles. Only a slight bending up observed in the experimental data of the hold profile does not seem to be well captured by the implemented model. This may indicate that a mechanism leading to the stabilization of the catalyst under steady-state conditions of the hold profile has been neglected by the model. However, apart from this aspect, based on the minimized low root mean squared error, a successful model fitting and therefore parameter estimation was achieved.

This set of parameters is then employed to predict the outcome of the other three PEMWE operation profiles that are presented in Figure 5 (triangle, sawtooth-up and sawtooth-down). The model simulations and the cor-



(a) Parameter estimation step: Normalized ECSA data from Alia [38] vs the simulated results from the model with the application of the temporal multiscale method (TMS) for hold and square-wave profiles.



(b) Model prediction step: Normalized ECSA data from Alia [38] vs the simulated results from the model with the application of the temporal multiscale method (TMS) for triangular, sawtooth-up and down profiles.

Figure 8: Slow-Scale variables results compared with the experimental data provided by [38] after 21 days of simulation.

responding data are presented in Figure 8 b). The model predictions show a significant deviation from the experimental data, indicating the need for further development and improvement of the mechanistic degradation model. In particular, the model appears to underestimate the degradation effect of the slower, dynamic ramps of the triangular and the two sawtooth operation profiles.

Finding the ‘right’ electrochemical model which fits all the dynamic operation profiles shown is out of the scope of this work. However, it is shown how the application of the temporal multiscale approach can lead to a much faster simulation of long-term degradation processes in PEMWE.

A systematic model development can be performed by iterating the following steps: 1) proposing/modifying the mathematical degradation model, 2) applying the parameter fitting procedure, 3) performing predictive simulations and 4) comparing the predictive simulations with the experimental data. The temporal multiscale approach can play an important role in this iterative process by facilitating the simulation and especially the parameter estimation step. Once a reliable degradation model is found, the temporal multiscale approach can also be used to optimize the dynamic operation of PEMWE, taking into account the long-term degradation effects of different

dynamic operation strategies.

Conclusion and future perspectives

In this work, a temporal multiscale method was applied to accelerate simulation of degradation in PEMWE under dynamic operating conditions. With an exemplary focus on the phenomenon of catalyst dissolution, a mechanistic degradation model was hypothesized and implemented. Due to the specific underlying temporal multiscale structure of the fully-resolved problem, its computational complexity was reduced by solving a temporal multiscale equivalent problem.

In this regard, two different temporal scales were identified: A fast process with quasi-local periodicity dictated by the transport and reaction processes occurring under intermittent operation conditions of PEMWE, and a slow process constituted by the gradual degradation of the catalyst layer.

Assuming that the Slow-Scale variables are minimally affected by the Fast-Scale variables in a time step significantly larger than the one used for the time discretization of the Fast-Scale variables, we can consider the Slow-Scale variables as fixed during the computation of the Fast-Scale solution. Additionally, the presented temporal multiscale method leverages the quasi-local periodicity of the Fast-Scale variables not computing all the time steps but rather the necessary ones to achieve such periodicity. This enables the integration of the Slow-Scale variable solution over the mentioned large time step, utilizing the Fast-Scale variables solutions for just one period of time to compute the gradient.

The computational effort is substantially reduced compared to the fully-resolved problem solution. The temporal multiscale method, as mentioned before, doesn't required computing all the Fast-Scale solutions but only up to reaching a quasi-local periodicity for each Slow-Scale large time step. This makes it possible to reduce simulations of 21 days from 8 computational days for the fully-resolved problem to approximately 20 minutes. Furthermore, the mean squared error committed by the temporal multiscale method is approximately 10^{-5} , making the impact of the assumptions negligible in terms of accuracy.

Numerical challenges, such as the stiffness of the Fast-Scale problem, were overcome by applying an implicit integration method using the Newton method. A semi-implicit integration method was also employed to ensure

the stability of the coupling between the hydrogen transport and the ACL degradation problem.

The model parameters were fitted using a Simulating Annealing algorithm. Although a gradient descent method was not utilized as the optimization method for the parameter fitting to avoid additional errors from applying a finite difference method for small values, the temporal multiscale approach proposed in this work also contributed to accelerating this procedure. Since the simulations took significantly less time than before, a wider search space of possible fitting solutions was explored. For this purpose, 128 simultaneous simulations were run for each iteration of the Simulating Annealing Method, resulting in a better approximation to the optimal parameters for fitting this problem. This could be replaced in the future by a fitting method that directly considers the particular temporal multiscale structure of the problem.

The Slow-Scale variables were investigated to analyse the electrochemical problem. The model parameters were estimated by fitting the model to the experimental data of two operation profiles ('hold' and 'square-wave') in PEMWE, resulting in a close agreement between the model simulation and the experimental data. However, the model prediction of the three other operation profiles ('triangular', 'sawtooth-up' and 'sawtooth-down') shows significant deviations from the experimental data, indicating the need for further modification of the mathematical degradation model.

In this paper, it is shown that the application of the temporal multiscale method can support the systematic development of a degradation model in PEMWE by drastically reducing the computational time for the model fitting and predictive simulation steps. In the future, the application of the temporal multiscale method can also aid to realize efficient numerical methods that can be used to optimize the dynamic operation of PEMWE.

Acknowledgements

The work of DD was supported by the Center of Dynamic Systems (CDS), funded by the EU-programme ERDF (European Regional Development Fund).

In addition to this support, this work was authored in part by the National Renewable Energy Laboratory, operated by Alliance for Sustainable Energy, LLC, for the U.S. Department of Energy (DOE) under Contract No. DE-AC36-08GO28308. The views expressed in the article do not necessarily

represent the views of the DOE or the U.S. Government. The U.S. Government retains and the publisher, by accepting the article for publication, acknowledges that the U.S. Government retains a nonexclusive, paid-up, irrevocable, worldwide license to publish or reproduce the published form of this work, or allow others to do so, for U.S. Government purposes.

References

- [1] M. Prestat, Corrosion of structural components of proton exchange membrane water electrolyzer anodes: A review, *Journal of Power Sources* 556 (2023) 232469. URL: <https://www.sciencedirect.com/science/article/pii/S037877532201446X>. doi:10.1016/j.jpowsour.2022.232469.
- [2] A. P. Dam, B. Y. A. Abuthaher, G. Papakonstantinou, K. Sundmacher, Insights into the path-dependent charge of iridium dissolution products and stability of electrocatalytic water splitting, *Journal of The Electrochemical Society* 170 (2023) 064504. URL: <https://dx.doi.org/10.1149/1945-7111/acd4f2>. doi:10.1149/1945-7111/acd4f2, publisher: IOP Publishing.
- [3] A. Voronova, H.-J. Kim, J. H. Jang, H.-Y. Park, B. Seo, Effect of low voltage limit on degradation mechanism during high-frequency dynamic load in proton exchange membrane water electrolysis, *International Journal of Energy Research* 46 (2022) 11867–11878. URL: <https://onlinelibrary.wiley.com/doi/abs/10.1002/er.7953>. doi:10.1002/er.7953, _eprint: <https://onlinelibrary.wiley.com/doi/pdf/10.1002/er.7953>.
- [4] X. Qian, K. Kim, S. Jung, Multiphase, multidimensional modeling of proton exchange membrane water electrolyzer, *Energy Conversion and Management* 268 (2022) 116070. URL: <https://www.sciencedirect.com/science/article/pii/S0196890422008573>. doi:10.1016/j.enconman.2022.116070.
- [5] A. P. Dam, G. Papakonstantinou, K. Sundmacher, On the role of microkinetic network structure in the interplay between oxygen evolution reaction and catalyst dissolution, *Scientific Reports* 10 (2020) 14140. URL: <http://www.nature.com/articles/s41598-020-69723-3>. doi:10.1038/s41598-020-69723-3.

- [6] J. Knöppel, M. Möckl, D. Escalera-López, K. Stojanovski, M. Bierling, T. Böhm, S. Thiele, M. Rzepka, S. Cherevko, On the limitations in assessing stability of oxygen evolution catalysts using aqueous model electrochemical cells, *Nature Communications* 12 (2021) 2231. URL: <http://www.nature.com/articles/s41467-021-22296-9>. doi:10.1038/s41467-021-22296-9.
- [7] S. A. Grigor'ev, M. M. Khaliullin, N. V. Kuleshov, V. N. Fateev, Electrolysis of Water in a System with a Solid Polymer Electrolyte at Elevated Pressure, *Russian Journal of Electrochemistry* 37 (2001) 819–822. doi:<http://dx.doi.org/10.1023/A:1016735003101>.
- [8] K. Onda, T. Murakami, T. Hikosaka, M. Kobayashi, R. Notu, K. Ito, Performance Analysis of Polymer-Electrolyte Water Electrolysis Cell at a Small-Unit Test Cell and Performance Prediction of Large Stacked Cell, *Journal of The Electrochemical Society* 149 (2002) A1069. URL: <https://iopscience.iop.org/article/10.1149/1.1492287>. doi:10.1149/1.1492287.
- [9] P. Olivier, C. Bourasseau, P. B. Bouamama, Low-temperature electrolysis system modelling: A review, *Renewable and Sustainable Energy Reviews* 78 (2017) 280–300. URL: <https://linkinghub.elsevier.com/retrieve/pii/S136403211730432X>. doi:10.1016/j.rser.2017.03.099.
- [10] S. A. Grigoriev, A. A. Kalinnikov, P. Millet, V. I. Porembsky, V. N. Fateev, Mathematical modeling of high-pressure PEM water electrolysis, *Journal of Applied Electrochemistry* 40 (2010) 921–932. URL: <http://link.springer.com/10.1007/s10800-009-0031-z>. doi:10.1007/s10800-009-0031-z.
- [11] T. Yigit, O. F. Selamet, Mathematical modeling and dynamic Simulink simulation of high-pressure PEM electrolyzer system, *International Journal of Hydrogen Energy* 41 (2016) 13901–13914. URL: <https://linkinghub.elsevier.com/retrieve/pii/S0360319916318341>. doi:10.1016/j.ijhydene.2016.06.022.
- [12] P. Trinke, B. Bensmann, S. Reichstein, R. Hanke-Rauschenbach, K. Sundmacher, Hydrogen permeation in PEM electrolyzer cells operated at asymmetric pressure conditions, *Journal of The Electrochemi-*

- cal Society 163 (2016) F3164–F3170. URL: <https://iopscience.iop.org/article/10.1149/2.0221611jes>. doi:10.1149/2.0221611jes.
- [13] G. Papakonstantinou, K. Sundmacher, H₂ permeation through n117 and its consumption by IrO_x in PEM water electrolyzers, *Electrochemistry Communications* 108 (2019) 106578. URL: <https://linkinghub.elsevier.com/retrieve/pii/S1388248119302413>. doi:10.1016/j.elecom.2019.106578.
- [14] T. Franz, G. Papakonstantinou, K. Sundmacher, Transient hydrogen crossover in dynamically operated PEM water electrolysis cells - A model-based analysis, *Journal of Power Sources* 559 (2023) 232582. URL: <https://www.sciencedirect.com/science/article/pii/S0378775322015592>. doi:10.1016/j.jpowsour.2022.232582.
- [15] A. Abdol Rahim, A. S. Tijani, S. Kamarudin, S. Hanapi, An overview of polymer electrolyte membrane electrolyzer for hydrogen production: Modeling and mass transport, *Journal of Power Sources* 309 (2016) 56–65. URL: <https://linkinghub.elsevier.com/retrieve/pii/S037877531630012X>. doi:10.1016/j.jpowsour.2016.01.012.
- [16] F. Aubras, J. Deseure, J.-J. Kadjo, I. Dedigama, J. Majasan, B. Grondin-Perez, J.-P. Chabriat, D. Brett, Two-dimensional model of low-pressure PEM electrolyser: Two-phase flow regime, electrochemical modelling and experimental validation, *International Journal of Hydrogen Energy* 42 (2017) 26203–26216. URL: <https://linkinghub.elsevier.com/retrieve/pii/S0360319917335565>. doi:10.1016/j.ijhydene.2017.08.211.
- [17] E. T. Ojong, J. T. H. Kwan, A. Nouri-Khorasani, A. Bonakdarpour, D. P. Wilkinson, T. Smolinka, Development of an experimentally validated semi-empirical fully-coupled performance model of a PEM electrolysis cell with a 3-D structured porous transport layer, *International Journal of Hydrogen Energy* 42 (2017) 25831–25847. URL: <https://linkinghub.elsevier.com/retrieve/pii/S0360319917334869>. doi:10.1016/j.ijhydene.2017.08.183.
- [18] T. L. Doan, H. E. Lee, S. S. H. Shah, M. Kim, C. Kim, H. Cho, T. Kim, A review of the porous transport layer in polymer electrolyte membrane water electrolysis, *International Journal of Energy Research* 45

- (2021) 14207–14220. URL: <https://onlinelibrary.wiley.com/doi/10.1002/er.6739>. doi:10.1002/er.6739.
- [19] N. Lin, J. Zausch, 1d multiphysics modelling of PEM water electrolysis anodes with porous transport layers and the membrane, *Chemical Engineering Science* 253 (2023) 117600. URL: <https://www.sciencedirect.com/science/article/pii/S0009250922001841>. doi:10.1016/j.ces.2022.117600.
- [20] A. Ni, M. Upadhyay, S. S. Kumar, H. Uwitonze, H. Lim, Anode analysis and modelling hydrodynamic behaviour of the multiphase flow field in circular PEM water electrolyzer, *International Journal of Hydrogen Energy* 48 (2023) 16176–16183. URL: <https://www.sciencedirect.com/science/article/pii/S0360319923000332>. doi:10.1016/j.ijhydene.2023.01.032.
- [21] H. Gorgun, Dynamic modelling of a proton exchange membrane (PEM) electrolyzer, *International Journal of Hydrogen Energy* 31 (2006) 29–38. URL: <https://linkinghub.elsevier.com/retrieve/pii/S0360319905000868>. doi:10.1016/j.ijhydene.2005.04.001.
- [22] F. Marangio, M. Santarelli, M. Calì, Theoretical model and experimental analysis of a high pressure PEM water electrolyser for hydrogen production, *International Journal of Hydrogen Energy* 34 (2009) 1143–1158. URL: <https://www.sciencedirect.com/science/article/pii/S0360319908016571>. doi:10.1016/j.ijhydene.2008.11.083.
- [23] M. Lebbal, S. Lecœuche, Identification and monitoring of a PEM electrolyser based on dynamical modelling, *International Journal of Hydrogen Energy* 34 (2009) 5992–5999. URL: <https://linkinghub.elsevier.com/retrieve/pii/S0360319909002018>. doi:10.1016/j.ijhydene.2009.02.003.
- [24] M. Espinosa-López, C. Darras, P. Poggi, R. Glises, P. Baucour, A. Rakotonrainibe, S. Besse, P. Serre-Combe, Modelling and experimental validation of a 46 kW PEM high pressure water electrolyzer, *Renewable Energy* 119 (2018) 160–173. URL: <https://linkinghub.elsevier.com/retrieve/pii/S0960148117311825>. doi:10.1016/j.renene.2017.11.081.

- [25] G. S. Ogumerem, E. N. Pistikopoulos, Parametric optimization and control for a smart Proton Exchange Membrane Water Electrolysis (PEMWE) system, *Journal of Process Control* 91 (2020) 37–49. URL: <https://linkinghub.elsevier.com/retrieve/pii/S0959152420302092>. doi:10.1016/j.jprocont.2020.05.002.
- [26] A. Dizon, J. Fornaciari, M. Rochow, A. Z. Weber, Sensitivity and effective parameterization of a multi-scale model of proton-exchange-membrane water electrolysis, *ECS Transactions* 104 (2021) 417. URL: <https://iopscience.iop.org/article/10.1149/10408.0417ecst/meta>. doi:10.1149/10408.0417ecst, publisher: IOP Publishing.
- [27] R. Ding, Y. Chen, Z. Rui, K. Hua, Y. Wu, X. Li, X. Duan, X. Wang, J. Li, J. Liu, Guiding the optimization of membrane electrode assembly in a proton exchange membrane water electrolyzer by machine learning modeling and black-box interpretation, *ACS Sustainable Chemistry & Engineering* 10 (2022) 4561–4578. URL: <https://doi.org/10.1021/acssuschemeng.1c08522>. doi:10.1021/acssuschemeng.1c08522, publisher: American Chemical Society.
- [28] A. A. Franco, P. Schott, C. Jallut, B. Maschke, A multi-scale dynamic mechanistic model for the transient analysis of PEFCs, *Fuel Cells* 7 (2007) 99–117. doi:10.1002/fuce.200500204, _eprint: <https://onlinelibrary.wiley.com/doi/pdf/10.1002/fuce.200500204>.
- [29] A. A. Franco, M. Gerard, Multiscale model of carbon corrosion in a PEFC: Coupling with electrocatalysis and impact on performance degradation, *Journal of The Electrochemical Society* 155 (2008) B367. URL: <https://iopscience.iop.org/article/10.1149/1.2838165/meta>. doi:10.1149/1.2838165, publisher: IOP Publishing.
- [30] A. A. Franco, S. Passot, P. Fugier, C. Anglade, E. Billy, L. Guétaz, N. Guillet, E. D. Vito, S. Mailley, Pt x Co y catalysts degradation in PEFC environments: Mechanistic insights: I. multiscale modeling, *Journal of The Electrochemical Society* 156 (2009) B410. URL: <https://iopscience.iop.org/article/10.1149/1.3056048/meta>. doi:10.1149/1.3056048, publisher: IOP Publishing.

- [31] L. F. L. Oliveira, S. Laref, E. Mayousse, C. Jallut, A. A. Franco, A multi-scale physical model for the transient analysis of PEM water electrolyzer anodes, *Physical Chemistry Chemical Physics* 14 (2012) 10215. URL: <http://xlink.rsc.org/?DOI=c2cp23300b>. doi:10.1039/c2cp23300b.
- [32] Y. Yang, W. Jaeger, M. Neuss-Radu, T. Richter, Mathematical modeling and simulation of the evolution of plaques in blood vessels, *J. of Math. Biology.* 72 (2016) 973–996. doi:10.1007/s00285-015-0934-8.
- [33] F. Brinkmann, M. Mercker, T. Richter, A. Marciniak-Czochra, Post-Turing tissue pattern formation: Advent of Mechanochemistry, *PLOS Computational Biology* (2018). doi:10.1371/journal.pcbi.1006259.
- [34] W. E. B. Engquist, The heterogenous multiscale methods, *Communications in Mathematical Sciences* 1 (2003) 87–132. doi:10.4310/CMS.2003.v1.n1.a8, publisher: International Press of Boston.
- [35] W. E. B. Engquist, X. Li, W. Ren, E. Vanden-Eijnden, Heterogeneous multiscale methods: A review, *Comm. Comput. Phys.* 2 (2007) 367–450.
- [36] V. Gravemeier, S. Lenz, W. A. Wall, Towards a taxonomy for multi-scale methods in computational mechanics: building blocks of existing methods, *Comp. Mech.* 41 (2008) 279–291.
- [37] S. Frei, T. Richter, Efficient approximation of flow problems with multiple scales in time, *Multiscale Modeling & Simulation* 18 (2020) 942–969. URL: <https://epubs.siam.org/doi/10.1137/19M1258396>. doi:10.1137/19M1258396.
- [38] S. M. Alia, S. Stariha, R. L. Borup, Electrolyzer durability at low catalyst loading and with dynamic operation, *Journal of The Electrochemical Society* 166 (2019) F1164–F1172. URL: <https://iopscience.iop.org/article/10.1149/2.0231915jes>. doi:10.1149/2.0231915jes.
- [39] A. Weiß, A. Siebel, M. Bernt, T.-H. Shen, V. Tileli, H. A. Gasteiger, Impact of Intermittent Operation on Lifetime and Performance of a PEM Water Electrolyzer, *Journal of The Electrochemical Society* 166 (2019) F487–F497. URL: <https://iopscience.iop.org/article/10.1149/2.0421908jes>. doi:10.1149/2.0421908jes.

- [40] O. Kasian, J. Grote, S. Geiger, S. Cherevko, K. J. J. Mayrhofer, The Common Intermediates of Oxygen Evolution and Dissolution Reactions during Water Electrolysis on Iridium, *Angewandte Chemie International Edition* 57 (2018) 2488–2491. doi:10.1002/anie.201709652, _eprint: <https://onlinelibrary.wiley.com/doi/pdf/10.1002/anie.201709652>.
- [41] S. Geiger, O. Kasian, M. Ledendecker, E. Pizzutilo, A. M. Mingers, W. T. Fu, O. Diaz-Morales, Z. Li, T. Oellers, L. Fruchter, A. Ludwig, K. J. J. Mayrhofer, M. T. M. Koper, S. Cherevko, The stability number as a metric for electrocatalyst stability benchmarking, *Nature Catalysis* 1 (2018) 508–515. URL: <https://www.nature.com/articles/s41929-018-0085-6>. doi:10.1038/s41929-018-0085-6, number: 7 Publisher: Nature Publishing Group.
- [42] T. Binniger, R. Mohamed, K. Waltar, E. Fabbri, P. Levecque, R. Kötz, T. J. Schmidt, Thermodynamic explanation of the universal correlation between oxygen evolution activity and corrosion of oxide catalysts, *Scientific Reports* 5 (2015) 12167. URL: <https://www.nature.com/articles/srep12167>. doi:10.1038/srep12167, number: 1 Publisher: Nature Publishing Group.
- [43] G. Papakonstantinou, I. Spanos, A. Phuc Dam, R. Schlögl, K. Sundmacher, Electrochemical evaluation of the de-/re-activation of oxygen evolving Ir oxide, *Physical Chemistry Chemical Physics* 24 (2022) 14579–14591. URL: <https://pubs.rsc.org/en/content/articlelanding/2022/cp/d2cp00828a>. doi:10.1039/D2CP00828A, publisher: Royal Society of Chemistry.
- [44] Q. Liu, P. Jiang, H. Xiang, Experimental and molecular dynamics study of gas flow characteristics in nanopores, *Chinese Science Bulletin* 57 (2012) 1488–1493. URL: <https://doi.org/10.1007/s11434-012-5088-0>. doi:10.1007/s11434-012-5088-0.
- [45] P. Trinke, B. Bensmann, R. Hanke-Rauschenbach, Current density effect on hydrogen permeation in PEM water electrolyzers, *International Journal of Hydrogen Energy* 42 (2017) 14355–14366. URL: <https://linkinghub.elsevier.com/retrieve/pii/S0360319917312971>. doi:10.1016/j.ijhydene.2017.03.231.

- [46] W. E, Principles of Multiscale Modeling, Cambridge University Press, 2011.
- [47] A. Abdulle, E. Weinan, B. Engquist, E. Vanden-Eijnden, The heterogeneous multiscale method, *Acta Numerica* 21 (2012) 1–87. doi:10.1017/S0962492912000025, publisher: Cambridge University Press.
- [48] L. Lautsch, T. Richter, Error Estimation and Adaptivity for Differential Equations with Multiple Scales in Time, *Computational Methods in Applied Mathematics* 21 (2021) 841–861. URL: <https://www.degruyter.com/document/doi/10.1515/cmam-2021-0030/html>. doi:10.1515/cmam-2021-0030, publisher: De Gruyter.
- [49] P. Virtanen, R. Gommers, T. E. Oliphant, M. Haberland, T. Reddy, D. Cournapeau, E. Burovski, P. Peterson, W. Weckesser, J. Bright, S. J. van der Walt, M. Brett, J. Wilson, K. J. Millman, N. Mayorov, A. R. J. Nelson, E. Jones, R. Kern, E. Larson, C. J. Carey, Í. Polat, Y. Feng, E. W. Moore, J. VanderPlas, D. Laxalde, J. Perktold, R. Cimrman, I. Henriksen, E. A. Quintero, C. R. Harris, A. M. Archibald, A. H. Ribeiro, F. Pedregosa, P. van Mulbregt, SciPy 1.0 Contributors, SciPy 1.0: Fundamental Algorithms for Scientific Computing in Python, *Nature Methods* 17 (2020) 261–272. doi:10.1038/s41592-019-0686-2.
- [50] D. R. Greening, Parallel simulated annealing techniques, *Physica D: Nonlinear Phenomena* 42 (1990) 293–306. URL: <https://www.sciencedirect.com/science/article/pii/0167278990900843>. doi:[https://doi.org/10.1016/0167-2789\(90\)90084-3](https://doi.org/10.1016/0167-2789(90)90084-3).